Earth and Planetary Science Letters 434 (2016) 308–319

Contents lists available at ScienceDirect

Earth and Planetary Science Letters

www.elsevier.com/locate/epsl

Multidisciplinary constraints of hydrothermal explosions based on the 2013 Gengissig lake events, Kverkfjöll volcano, Iceland

Cristian Montanaro [a,*], Bettina Scheu [a], Magnus Tumi Gudmundsson [b], Kristín Vogfjörd [c], Hannah Iona Reynolds [b], Tobias Dürig [b], Karen Strehlow [d], Stefanie Rott [a], Thierry Reuschlé [e], Donald Bruce Dingwell [a]

[a] Department of Earth and Environmental Sciences, Ludwig-Maximilians-Universität München, Theresienstrasse 41/III, 80333 Munich, Germany
[b] Nordic Volcanological Center, Institute of Earth Sciences, University of Iceland, Sturlugata 7, IS-101 Reykjavik, Iceland
[c] Icelandic Meteorological Office, 150 Reykjavík, Iceland
[d] School of Earth Sciences, University of Bristol, Wills Memorial Building, Queen's Road, Clifton BS8 1RJ, Bristol, United Kingdom
[e] Ecole et Observatoire des Sciences de la Terre, Institut de Physique du Globe de Strasbourg, 5 rue René Descartes, 67084 Strasbourg Cedex, France

ARTICLE INFO

Article history:
Received 18 June 2015
Received in revised form 25 November 2015
Accepted 27 November 2015
Available online 14 December 2015
Editor: T.A. Mather

Keywords:
hydrothermal explosions
lake drainage
multidisciplinary
deposits volume
energy partitioning

ABSTRACT

Hydrothermal explosions frequently occur in geothermal areas showing various mechanisms and energies of explosivity. Their deposits, though generally hardly recognised or badly preserved, provide important insights to quantify the dynamics and energy of these poorly understood explosive events. Furthermore the host rock lithology of the geothermal system adds a control on the efficiency in the energy release during an explosion. We present results from a detailed study of recent hydrothermal explosion deposits within an active geothermal area at Kverkfjöll, a central volcano at the northern edge of Vatnajökull. On August 15th 2013, a small jökulhlaup occurred when the Gengissig ice-dammed lake drained at Kverkfjöll. The lake level dropped by approximately 30 m, decreasing pressure on the lake bed and triggering several hydrothermal explosions on the 16th. Here, a multidisciplinary approach combining detailed field work, laboratory studies, and models of the energetics of explosions with information on duration and amplitudes of seismic signals, has been used to analyse the mechanisms and characteristics of these hydrothermal explosions. Field and laboratory studies were also carried out to help constrain the sedimentary sequence involved in the event. The explosions lasted for 40–50 s and involved the surficial part of an unconsolidated and hydrothermally altered glacio-lacustrine deposit composed of pyroclasts, lavas, scoriaceous fragments, and fine-grained welded or loosely consolidated aggregates, interbedded with clay-rich levels. Several small fans of ejecta were formed, reaching a distance of 1 km north of the lake and covering an area of approximately 0.3 km^2, with a maximum thickness of 40 cm at the crater walls. The material (volume of approximately 10^4 m^3) has been ejected by the expanding boiling fluid, generated by a pressure failure affecting the surficial geothermal reservoir. The maximum thermal, craterisation and ejection energies, calculated for the explosion areas, are on the order of 10^{11}, 10^{10} and 10^9 J, respectively. Comparison of these with those estimated by the volume of the ejecta and the crater sizes, yields good agreement. We estimate that approximately 30% of the available thermal energy was converted into mechanical energy during this event. The residual energy was largely dissipated as heat, while only a small portion was converted into seismic energy. Estimation of the amount of freshly-fragmented clasts in the ejected material obtained from SEM morphological analyses, reveals that a low but significant energy consumption by fragmentation occurred. Decompression experiments were performed in the laboratory mimicking the conditions due to the drainage of the lake. Experimental results confirm that only a minor amount of energy is consumed by the creation of new surfaces in fragmentation, whereas most of the fresh fragments derive from the disaggregation of aggregates. Furthermore, ejection velocities of the particles (40–50 m/s), measured via high-speed videos, are consistent with those estimated from the field. The multidisciplinary approach used here to investigate

* Corresponding author.
E-mail address: cristian.montanaro@min.uni-muenchen.de (C. Montanaro).

http://dx.doi.org/10.1016/j.epsl.2015.11.043

hydrothermal explosions has proven to be a valuable tool which can provide robust constraints on energy release and partitioning for such small-size yet hazardous, steam-explosion events.

1. Introduction

Unrest in geothermal areas can be manifested in jetting or eruption of hydrothermal fluids (steam, water) and substantial amounts of solid material (mud and rock fragments). Such events are commonly referred to as hydrothermal explosions, a type of non-juvenile eruption, or "boiling-point eruption" (Mastin, 1995). The term "explosion" is here used as opposed to "eruption" following the terminology presented in Muffler et al. (1971). Hydrothermal explosions can last from seconds to hours (Browne and Lawless, 2001; Jolly et al., 2014), and produce craters spanning from a few meters up to more than 2 km in diameter, with depths from few meters to several hundred meters strongly dependent on host rock composition (Muffler et al., 1971; Browne and Lawless, 2001). Typical eruptive velocities vary between few tens of m/s up to more than 200 m/s (Browne and Lawless, 2001; Kilgour et al., 2010; Breard et al., 2014). Deposits are generally of low volume ($<10^5$ m^3); they are typically very-poorly sorted, matrix-supported, and may contain hydrothermally altered clasts from the geothermal reservoir (Muffler et al., 1971; Mastin, 1995; Browne and Lawless, 2001).

Hydrothermal explosions are common in many volcanic terrains as well as other areas of high heat flow, where abundant hydrothermal activity favours conditions for rapid generation of steam and pressure build-up. Despite their frequent occurrence (Barberi et al., 1992; Browne and Lawless, 2001), these eruptions are still poorly understood. Their deposits are often not recognised, badly preserved or buried under younger materials. In addition the dynamics and magnitude of such eruptions tends to be unpredictable. Recent hydrothermal eruptions at Mt. Ontake in Japan (Yamamoto, 2014; Kato et al., 2015), and Ruapehu and Te Maari, in New Zealand (Kilgour et al., 2010; Breard et al., 2014), highlight major proximal hazards of these events. Moreover they occurred with little or no pre-eruptive monitoring signals (Hurst et al., 2014).

The conditions that cause hydrothermal explosions arise through a rapid increase in temperature or decrease in pressure. The contained fluids may flash to steam, resulting in significant volume increase and fragmentation of the enclosing rocks (Smith and McKibbin, 2000; McKibbin et al., 2009). The heating is the result of an increase in reservoir energy, (e.g. by injection of magma or magmatic gases), as in the recent Mt. Ontake eruption (Kato et al., 2015). Pressure reduction can arise due to removal of fluid from a geothermal area, for instance by exploitation, or a reduction in confining pressure by a landslide (e.g. Te Maari eruption; Breard et al., 2014), erosion processes, lowering of groundwater, or rapid draining of an overlying lake (Muffler et al., 1971). The response of a reservoir to rapid decompression depends mostly on its permeability. Highly permeable reservoirs are likely to efficiently release any steam generated, thus largely preventing pressure build-up and explosions. However, if such a reservoir is capped by low-permeable layers, steam generated may not escape and pressurization of the reservoir is likely; sufficient pressurization may cause rupture of the capping layers and thus initiate rapid depressurization and explosions (Browne and Lawless, 2001; Seki et al., 2015).

The rate at which energy is released controls the violence of such explosions. This depends on 1) the physical condition (P-T) of a system before the explosion (Mastin, 1995), and 2) the nature of the rock hosting the geothermal system (Muffler et al., 1971; Browne and Lawless, 2001). Here a multidisciplinary approach was chosen to study the mechanisms and the energetics of small-sized hydrothermal explosions occurring on August 16th, 2013 at Kverkfjöll, Iceland. These explosions were associated with a sudden drainage of an ice-dammed lake and represent a low-energy end-member case compared with the recent hydrothermal eruptions at Mt. Ontake in Japan (Yamamoto, 2014), and Te Maari, in New Zealand (Lube et al., 2014). The latter involved different mechanisms and also larger volumes, durations, products and types of confining rock. The Kverkfjöll event presents a unique opportunity to shed light on this low-energy hydrothermal explosion type. We combine detailed field surveys, sampling of deposits, laboratory studies, and analytical models with seismic data to define their characteristics, and understand the role of host-rock involved in the explosions.

2. Geological setting

The Kverkfjöll central volcano is a mountain massif with a relief of 1200 m, located in central Iceland, at the northern margin of Vatnajökull glacier. The southern part is mostly ice covered, including two calderas (Fig. 1). Generally Kverkfjöll eruptive products are basaltic with lithologies dominated by pillow lava, hyaloclastite, and fine-grained tuffs (Óladóttir et al., 2011). No volcanic eruptions are known to have occurred in the last 1100 yrs but several moderate-sized explosive basaltic eruptions have occurred in the Holocene (Óladóttir et al., 2011), which have been the source of catastrophic pre-historic floods (Carrivick et al., 2004). The geothermal activity is mostly concentrated along a SSW–NNE trending lineament, cutting through the volcano (Thorarinsson, 1953; Ólafsson et al., 2000). A 500–600 m wide and 100 m deep depression is located in the centre of the active area, about 500–1000 m east of the main lineation. This depression exhibit vigorous thermal activity and the ice-dammed lake Gengissig. The lake is characterized on the northern shore by a geothermal field enclosed by ice (Fig. 1). Here a number of (near-) boiling hydrothermal pools, sulphurous fumaroles, hot springs, and geothermal sediments are present.

3. August 16th hydrothermal explosions

On August 15th 2013, a small jökulhlaup occurred when the Gengissig ice-dammed meltwater lake drained at Kverkfjöll (Gudmundsson et al., 2013). The lake level dropped 30 m to 1607 m a.s.l. in 10–15 hrs (estimated from the discharge at a gauging station in river Jökulsá, 40 km downstream from the glacier margin, and eyewitness observations of the jökulhlaup: B. Einarsson pers. communication). Wardens at a nearby hut noted that the water level in the short tributary river Volga issuing from the glacier margin about 7 km north of Gengissig was rising on August 15th between 20:30 and 23:00. On August 16th at 07:30 the river discharge was still relatively high but had subsided considerably, indicating that the draining event had waned by that time. This was confirmed by a Coast Guard helicopter inspection flight in the afternoon of the 16th of August. The decompression beneath the lake bed, calculated to be 4–8 Pa/s (head loss of 20–30 m over 10–15 hrs), likely triggered the rapid boiling in the surficial geothermal reservoir. Subsequent to this event hydrothermal explosions occurred, producing several fans of ejecta dispersed over 1 km from the lake by southerly winds. Craters, up to 30–40 m

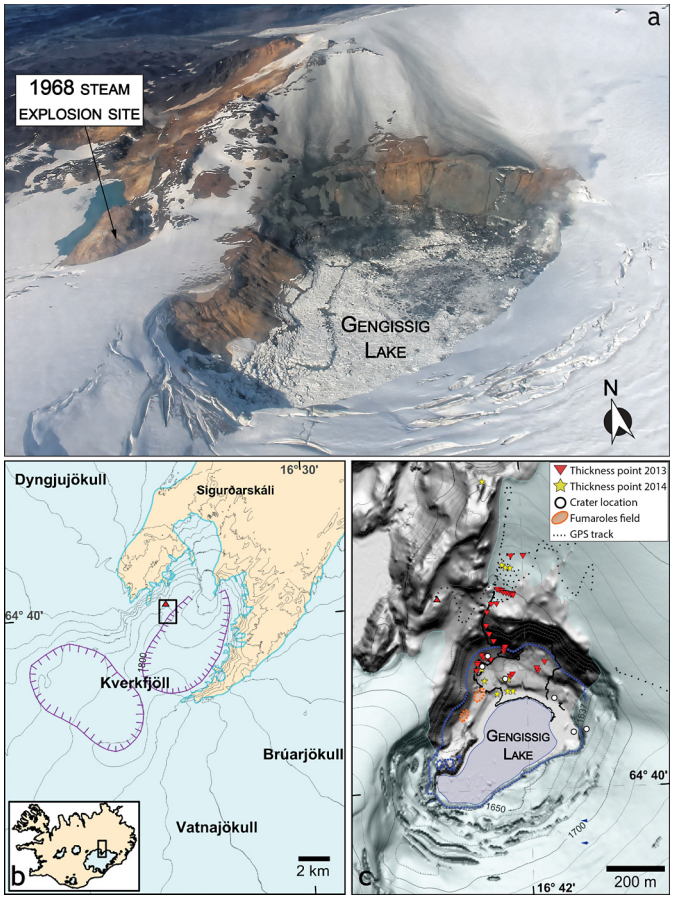

Fig. 1. (a) Aerial photo of Gengissig lake on the 16th of August 2013; several small fans of ejecta are visible north of the lake to a distance of about 1 km. A debris blanket characterizes the area in proximity of the craters. Steaming activity is also visible at the crater sites, especially on the north-eastern side of the lake area. (b) Map of Kverkfjöll caldera. (c) Lidar map of Gengissig lake area, marked by a black rectangle in (b). Dashed and continuous blue lines represent the lake level before (1637 m) and after (1607 m) the drainage. (For interpretation of the references to colour in this figure legend, the reader is referred to the web version of this article.)

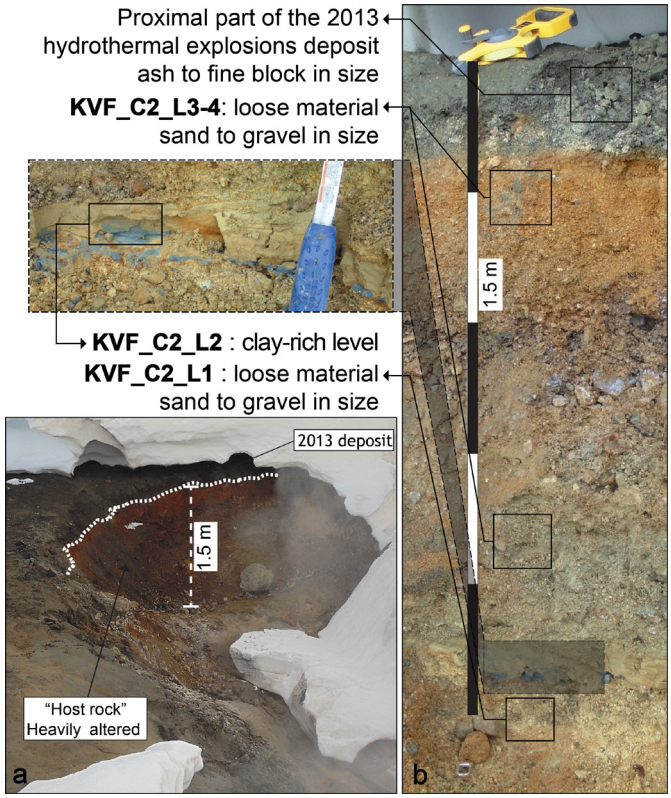

Fig. 2. (a) The rim of crater 2; the white dotted line marks the pre-explosion surface. (b) The 1.5 m thick section studied: the black–grey layer at the top of the section is the proximal part of the 2013 deposit. Areas highlighted by square boxes indicate the portions where samples of the Gengissig sedimentary succession and the deposit of the hydrothermal explosions were taken for analyses.

in diameter and partially-coalesced, were formed on the northern corner of the Gengissig depression along the pre-drainage shore line. Smaller, isolated craters were generated closer to the deeper part of the lake depression (Fig. 1). These explosions occurred in areas where the presence of fumarole systems and boiling pools suggest a high local heat flow.

Similar hydrothermal explosions occurred in Gengissig after a draining event in 1959 (Jóhannsson, 1959). In May 1968 a steam eruption occurred on the top of a hill 500 m west of Gengissig lake (Fig. 1; Thorarinsson, 1968). Gengissig lake has drained catastrophically in jökulhlaups at least five times in the 30 yrs prior to 2013: in 1985, 1987, 1993, 1997 and 2002. However, it is not known whether explosions were associated with these drainage events (Gudmundsson and Högnadóttir, 2009).

4. Field-based studies

A preliminary study of the eruptive products of the 16th August explosions was carried out by an aerial reconnaissance survey on the following day (Fig. 1). On 28th, we conducted an initial field campaign to sample and measure the deposit thicknesses before burial by snowfall. Additionally, boundaries of ejecta fans and the crater area were mapped with kinematic GPS. Nine months later, when a few meters of snow had largely buried the fresh deposits, we conducted a second campaign to re-examine the proximal deposits and the stratigraphic sequence involved in the explosions. In both campaigns we collected samples for component and grain-size analyses, particle shape characterization and density measurements. Field observations were then used to reconstruct the explosion scenario, estimate the volume of ejected material, and evaluate the energy partitioning in these small-size events.

4.1. Gengissig sedimentary succession

A sedimentary succession of hydrothermally altered glaciolacustrine unconsolidated deposit covered the depression occupied by Gengissig lake (Ólafsson et al., 2000). Alteration minerals are dominantly heulandite (Ca/Na zeolite) and smectite (Fe/Mg phyllosilicates), with lesser amounts of gypsum, quartz, sulphur, jarosite, and pyrite (Cousins et al., 2013). Investigation of erosional features and the study of the exposed outcrops at the crater walls enabled a more detailed overview of the succession involved in the explosions. However, there is still a lack of detailed studies (drilling, stratigraphy etc.) concerning the subsurface structure of the Gengissig area.

Two representative outcrops from the larger coalescent craters and a smaller crater (craters 2–3 in Figs. 2 and 3) were analysed in detail. Both successions comprise poorly sorted, matrix-supported sand to gravel in layers of sub-angular to sub-rounded clasts. These coarser layers, are interbedded with clay-rich levels (Fig. 2 and Figs. 1–2 suppl. mat.). The main components of the coarse fraction have basaltic lithologies varying from lavas to scoriaceous fragments, and fine-grained welded or loosely consolidated aggregates, composed of fine glass fragments and alteration minerals. The clay-rich levels (10 to 15 cm thick) vary in colour from bluish to yellowish when altered and locally show relative enrichments in sand and gravel.

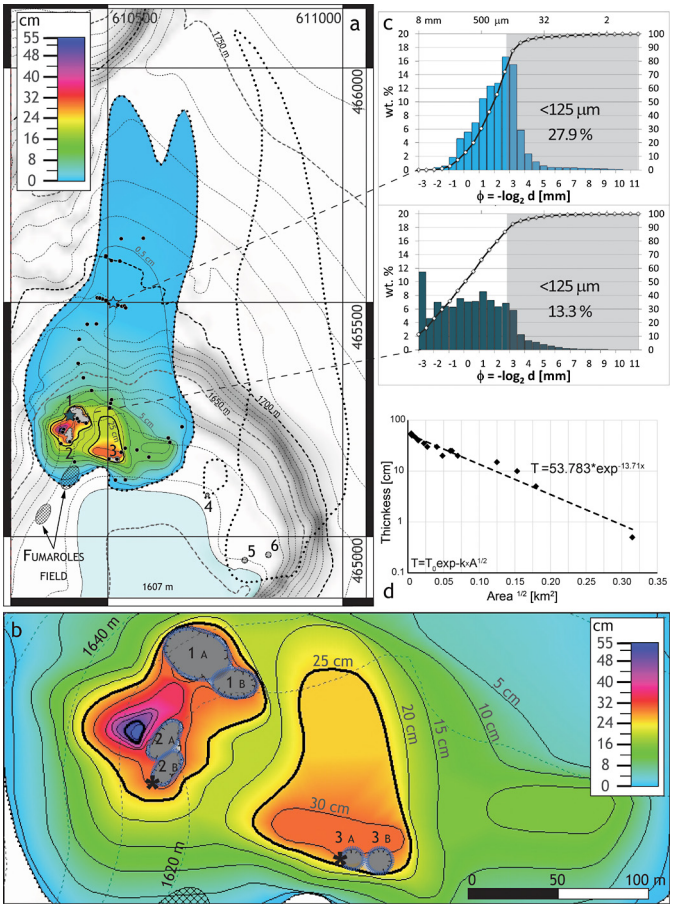

Fig. 3. (a) Isopach map of the 2013 hydrothermal explosions; crater locations labelled 1 to 6. Black dots denote thickness measurement points. (b) Close-up of area with craters 1–3. Hashed lines indicate crater margins, used for volume and energy calculations. Asterisks indicate the position of the outcrops at craters 2 and 3 described in the text. (c) Grain size distribution for proximal and mid-distal deposits. Stars in (a) show sampling site locations. (d) Semi-log plot showing deposit thickness as a function of square root of isopach area.

The north-western part of the studied area, together with an isolated area in the central part of the lake depression, exhibits varying grades of hydrothermal alteration. These areas correspond with fumarolic activity implying its role in the alteration process. In some areas alteration is limited to below a certain depth, where clay-rich levels appear to act as barriers.

4.2. Hydrothermal explosions deposit and crater features

Deposits of the hydrothermal explosions covered an area of approximately 0.3 km^2 and were dispersed towards the north forming three elongated fans. The westernmost and central fans were accessible and investigated in detail. The extent of the inaccessible proximal part of the eastern fan was mapped on the plateau (Fig. 3a).

The two studied fans covered approximately 0.15 km^2 with a maximum deposit thickness of 40 cm at the crater wall. Deposits thinned rapidly, to approximately a tenth, within 50–100 m from the crater rim (Fig. 3a). Most of the massively-bedded debris blanket consists of lapilli- and fine block-sized clasts ballistically emplaced around the crater areas. A minor amount of ash and lapilli was dispersed by winds to form elongated fans. The deposit reflects the composition of the underlying sequence including variably hydrothermally-altered lava lithics, intensely altered rock fragments, and recycled scoria and pumiceous clasts.

Several craters were formed following the explosions (Figs. 1, 3). Crater diameters on the north western side (no. 1–3) range from 9 to 24 m (Table 1). Sizes of the craters (no. 4–6) on the eastern side could not be determined. The craters exhibit two main morphologies: (1) larger craters on the north-western side characterized by irregular shapes, and (2) smaller isolated craters in the deeper part of the lake depression associated with a more circular form. The investigated craters were located at ca. 1617 m a.s.l. (ca. 20 m below the initial lake level).

4.3. Grain-size distribution

Grain-size distributions of the sedimentary succession and the hydrothermal explosion deposits were determined using dry sieving for the coarse fraction (>250 µm), and laser refraction technique using a Coulter LS230 (measuring range 0.375–2000 µm), for the fine fractions (<250 µm).

The coarser component of the sedimentary succession includes poorly sorted material with a polymodal distribution and maximum peaks around 4 and 8 mm; larger clasts in the succession represented a negligible percentage and were not considered. The clay-rich levels are better sorted with a modal peak between 250 and 100 µm (Figs. 1–2 suppl. mat.).

Samples from proximal and distal deposits of the hydrothermal explosions exhibit different grain-size distributions reflecting two different inferred emplacement mechanisms (Fig. 3). The very-poorly sorted proximal deposits show a polymodal distribution with the highest peak in the very coarse component (Figs. 3c and 3 suppl. mat.). Most of the material is in the ash to fine block range (<10 cm) and their distribution is used for the energy calculation. Several decimetre-sized lava blocks (up to 40 cm) are also present, but not included in the grain-size distribution as they represent a minor to negligible percentage of the overall deposit. In contrast, the mid-distal deposits are characterized by a more unimodal distribution with a peak around 180 µm (Figs. 1 and 3 suppl. mat.).

4.4. Particle shape characterization

A qualitative estimation of the amount of freshly-fragmented clasts in the ejected material was performed by using Scanning Electron Microscopy (SEM). SEM analysis shows the presence of

Table 1
Deposit volume, craters size data, and energy estimations.

Crater	D_{mean} (m)	Vol (m^3)	Err (m^3)	Foc. depth (m)	Err (m)	E_{Th} (J)	Err (J)	E_{Crat}[a] (J)	Err (J)	E_{Kin}[b] (J)	Err (J)
1 A	20.2	4600	684	21.5	3	1×10^{11}	1.5×10^{10}	3×10^{10}	5×10^{9}	9×10^{9}	2×10^{9}
1 B	13.3	1430	−195	15.5	−2	3×10^{10}	4×10^{9}	9×10^{9}	1×10^{9}	3×10^{9}	7×10^{8}
2 A	12.4	1180	−199	14.7	−2.5	2.4×10^{10}	4.5×10^{9}	7×10^{9}	1×10^{9}	2.4×10^{9}	5×10^{8}
2 B	10.6	765	−70	11.2	−1	1.6×10^{10}	1.6×10^{9}	4×10^{9}	4×10^{8}	1.9×10^{9}	4×10^{8}
3 A	8	350	/	20.9	/	8×10^{9}	/	2×10^{9}	/	7×10^{8}	1×10^{8}
3 B	9	485	/	23	/	9.9×10^{9}	/	3×10^{9}	/	9×10^{8}	2×10^{8}

[a] The E_{Crat} has been calculated based on the method of Goto et al. (2001).
[b] The E_{kin} represent an average of two values measured considering an initial ejection velocity of 40 and 50 m, respectively.

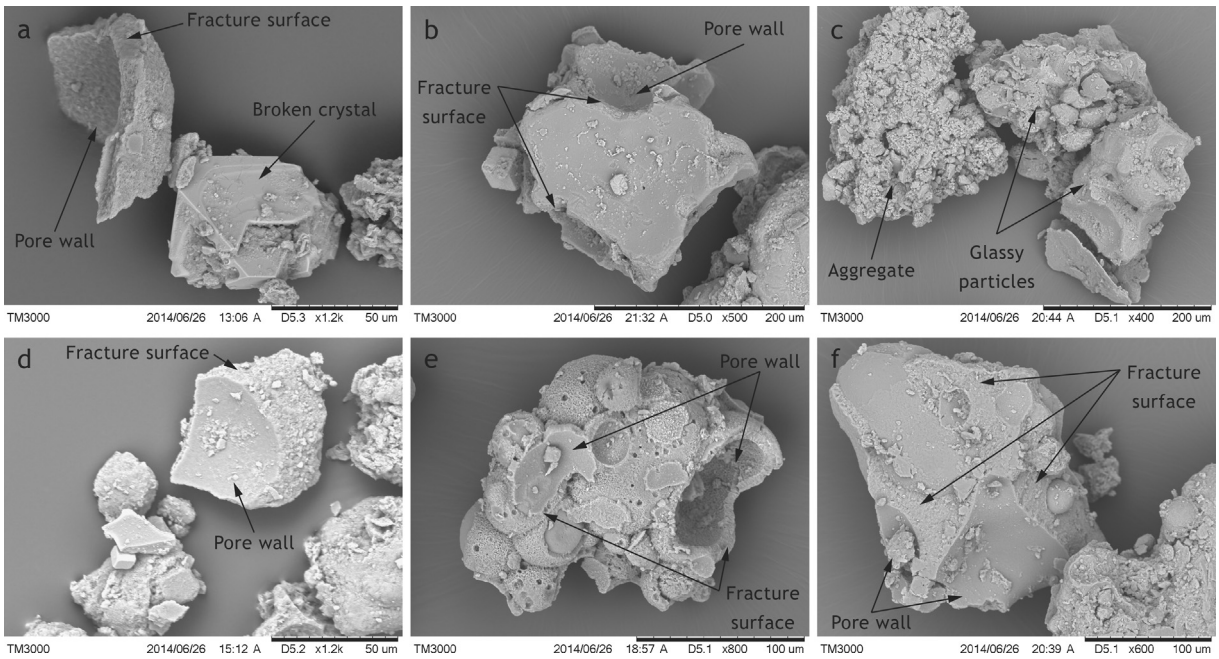

Fig. 4. SEM images showing: (a) crystal and glassy particle showing fresh fractures; (b) glassy particle with fresh fractures; (c) aggregate and glassy particle showing old fracture around pore wall; (d) glassy particle showing fresh fractures around pore wall and secondary alteration minerals; (e) alteration minerals aggregate with fractures around some of the pore walls; (f) glassy particle showing fresh fracture around pore walls.

non-juvenile particles only, characterized by a variety of surface morphologies and particle shapes. We identified four subgroups, the first of which is composed of blocky lithic grains, with more or less equant shapes showing a variable proportion of vesicles, small microlites, signs of chemical pitting and strong hydrothermal alteration (Fig. 4). Hydrothermal minerals clustered in a highly variant shape, from spherical to "agglutinate" in profile, form a second and predominant subgroup which we refer to as aggregates (Fig. 4c, e). SEM images that show particles in different stages of hydrothermal alterations indicate that the two further subpopulations exist: spherical amygdule vesicle-infillings and pure crystals (Fig. 4a, d, e). A minor but significant amount of fresh fracture surfaces were found on both, lithics and agglutinates. While it was beyond the scope of this study, a quantitative approach could be used to determine the proportion of different grain types.

4.5. Particle volume and mass

The volume of ejecta produced by the 16th August event was calculated using three different approaches.

Firstly, the volume was determined by measuring the deposit thickness at various locations across and down the main northward-directed dispersal axis. Based on the direct integration of the isopach map (Fig. 3a, d), the minimum volume of the deposits is estimated to be approximately 6×10^3 m^3.

The second method; exponential decay of deposit thickness away from the craters (Pyle, 1989) is approximated by a straight line on the semi-log plot of thickness vs. the square root of the area (Fig. 3). The extrapolated T_0 (maximum thickness at area equal 0) and the rate of thinning measured by $b_t = \ln 2/(k \times \pi^{1/2})$, where k is the line slope (Pyle, 1989), were then used to calculate the volume:

$$V = T_0 \times 13.08 \times b_t^2 \quad (1)$$

to yield a volume of 7×10^3 m^3.

A third estimation of the deposit volume was obtained according to the method of Sato and Taniguchi (1997), which is based on the relationship between crater diameter (R) and ejecta volume (V):

$$R = 0.97 \times V^{0.36} \quad (2)$$

This relationship was used to estimate the volume for each recognised crater and yields 8×10^3 m^3 (Table 1).

That all three volume estimates are quite consistent, probably reflects the fact that 1) most of the ejected material was deposited ballistically around the craters with little effect of wind dispersion (Pyle, 1989), and 2) the models yield better results with shallow events (Sato and Taniguchi, 1997; Goto et al., 2001). Assuming a field-measured bulk density of the ejected material of 1.1 g/cm^3, the calculated mass is thus c.$7.3 \pm 1 \times 10^6$ kg.

5. Seismic studies

Seismic monitoring of the Kverkfjöll caldera and other volcanoes in Iceland is operated by the Icelandic Meteorological Office (IMO). The network consists of mostly short period (Lennartz 5 s) stations, but in the Vatnajökull area several broad band stations are present (TRC20 20 s, Guralp 30 s, 60 s and 120 s). Real-time events recorded at the stations are automatically located and their magnitude is estimated within minutes of their occurrence. In August 2013 the closest station was at 19 km distance from Kverkfjöll, with 10 additional stations within 64 km (Fig. 5a). An explosion event was recorded on 16th August at 10 stations, very emergent and well above noise level (Fig. 5b). The signal appeared as a short tremor burst and therefore difficult to locate. An approximate location of roughly 2 km northeast of the explosion craters was obtained from the first arrivals at the three closest stations (kre, dyn, mko). The onset of the event was approximately 00:46:57. A continuous seismic trace from noon on the 14th of August at the closest station (kre) shows no other event of comparable amplitude that is not a confirmed earthquake elsewhere. The timing of the seismic signals and the observations at the glacier margin mentioned earlier, suggest that most of the water had already drained from the lake in the early hours of the 16th and that maximum flow occurred at the glacier edge during the night.

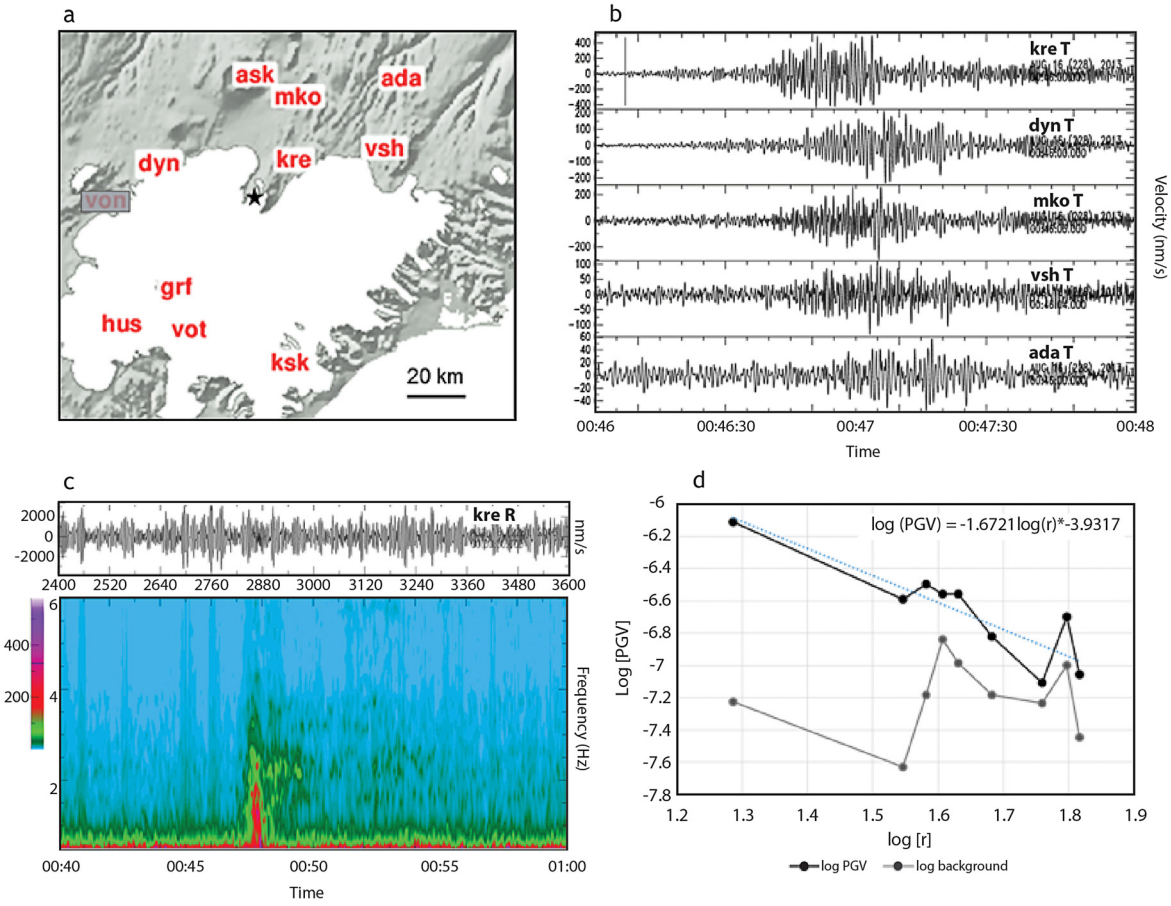

Fig. 5. (a) Map of Vatnajökull ice cap and Kverkfjöll (star) showing the location of seismic stations recording the Gengissig hydrothermal explosions. Amplitudes are in nm/s. (b) Two minutes of seismic records of radial component from 5 stations located at increasing distances from Kverkfjöll (from 19 to 64 km). Amplitudes are in nm/s and the data has been band-pass filtered between 1 and 7 Hz. (c) Twenty-minute-long, unfiltered tangential component seismogram from station kre, at 19 km distance from Kverkfjöll and its amplitude spectrogram, showing frequencies between 0.5 and 6 Hz. The figure shows the duration of the main explosions and the frequency content between 0.5 and 4 Hz. Below 0.5 Hz the signal is lost in the microseismic noise which dominates the seismogram. (d) Decay of peak ground velocity with distance from Kverkfjöll (solid black) and noise (solid grey). The best fitting line matches the linear part of the attenuation relation (Pétursson and Vogfjörd, 2012).

Characteristics of the signal from the closest seismic station (kre) indicate a duration of 40–50 s (spectrogram in Fig. 5c). Possibly smaller events, of shorter (10 s) duration, followed for another 1.5 min. Therefore most of the energy appears to be released in the first explosion. Amplitudes are too small to be seen above the micro-seismic noise, so the signals are only observed at frequencies higher than 0.5 Hz. Most of that energy is concentrated between 0.5 and 2.5 Hz, but frequencies of up to 4 Hz are observed. Tremor bursts in his frequency range are commonly observed on the seismic network during subglacial floods, reflecting the low-frequency source and the dominance of surface waves due to the shallow source depth (Vogfjörd et al., 2013). The smaller events are poorer in lower frequencies and peak around 2.1 Hz. A faint tail of elevated tremor, possibly reflecting vigorous boiling following the explosions, is observed for several minutes following the initial energetic events.

Peak ground velocities (PGV) and their decay with distance is shown in Fig. 5d together with the noise level for comparison. To estimate the seismic moment (M_0) for the event, the peak amplitudes were fitted to an attenuation relation between PGV and moment magnitude (M_W) derived for earthquakes in Iceland (Pétursson and Vogfjörd, 2012). The median of the moment magnitude estimates from each station indicates a $M_W = 1$ and seismic moment $M_0 = 4 \times 10^{10}$ N m. However, considering that similar magnitude and shallow earthquake sources located at Kverkfjöll are usually only 10–15 s long at station kre, while the event is of 40–50 s duration, the cumulative seismic moment for the event is estimated to be $4 \times M_0 \sim 1.6 \times 10^{11}$ N m.

Estimation of seismic energy (E_S) radiated by the explosion was obtained using a relation between the seismic moment and energy, $E_S = M_0 \times 10^{-4.8}$ (Choy and Boatwright, 1995). The relationship holds for many orders of magnitudes, different data sets and different regions, revealing a large spread in the data around the regression fit (Choy and Boatwright, 1995; Choy et al., 2006), and representing a rough estimate of the energy. By assuming $E_S/M_0 \sim 10^{-6}$–10^{-4}, and considering that the event is dominated by low frequencies, we expect the radiated energy to be on the lower end of the range, giving the estimate $E_S \sim 10^6$ J.

6. Laboratory studies

We analysed the permeability of samples taken during the field campaigns, with special focus towards the clay-rich levels observed in the successions (Fig. 2 and Figs. 1, 2 suppl. mat.). Additionally, we explored if these clay levels are likely to act as capping layers to area below, enhancing the pressure build-up during the explosions. Further, we conducted decompression experiments mimicking the conditions created during lake drainage to investigate the ejection dynamics as well as potential changes in the grain-size of the ejected particles due to fragmentation and compared the results with field-based information.

6.1. Permeability measurements

Water permeability measurements were conducted in a steady-state permeameter. The unconsolidated samples were placed in a stiff rubber jacket, carefully saturated with water and compacted under a uniaxial pressure of 0.3 MPa, corresponding to the in-situ pressure before the lake drainage. This procedure resulted in fragile but coherent cylindrical samples with a diameter of 20 mm and lengths ranging from 30 to 40 mm. The fluid volume flux was measured during steady state flow at a confining pressure of 0.3 MPa and four different water differential pressures ranging from 0.02 to 0.1 MPa. Permeability was derived from the flux measurements by using Darcy's law (de Marsily, 1986).

Two partially-altered clay-rich samples collected from 10 to 15 cm thick layers at the crater 2 and 3 (Figs. 2, 3 and Fig. 1 suppl. mat.), and one relatively unaltered sample close to the rim of crater 3 were investigated. The sample from crater 2 shows a bluish, clay-rich component in the lower part of the level, and a more sandy-rich portion in the upper part. The clay sample from crater 3 is less enriched in sand than the sample from crater 2. The third sample however, consists mainly of clay and is more homogeneous than the other two samples. From each of these, three sub-samples were analysed for permeability in order to check the repeatability of the obtained values (Table 1 suppl. mat.). We obtained permeability values of 2.3×10^{-14} m^2 and 3.8×10^{-15} m^2 for the sand-enriched clay levels, sampled at crater 2 and 3, respectively. The homogeneous clay-rich sample has a lower permeability of 1.2×10^{-17} m^2, due to its high clay content.

To explore the capability of these different clay level to act as barrier enhancing the pressure build-up, we consider the following assumptions: 1) the lake drainage caused a pressure decrease on the lake bottom sediments of approximately 2 bars (ca. 20 m of water column above the crater area; see section 4.2); 2) the decompression triggered the boiling of the fluids within the lake sediments (see section 8); 3) the time needed to release the boiling vapour pressure through these clay-rich levels is controlled by their permeability and thickness, according to a simple Darcian upflow (de Marsily, 1986). Thus the calculated flowing time through the sand-enriched levels ranges between 2 and 3 hours using the first permeability value reported above, and between 11 and 16 hrs using the second value. However, the permeability value for the clay-rich level equates to a drainage time ranging between 150 and 200 days. Accordingly, and considering the lake drainage duration (10–15 hrs), we speculate that the clay-rich levels (including those slightly enriched in sand) likely acted as a barrier to fluid flow prior and/or during the hydrothermal explosions due to their significantly longer flowing time.

6.2. Decompression experiments

6.2.1. Methods

We conducted rapid decompression experiments on particle–water mixtures using the shock-tube apparatus at LMU, described in detail by Alidibirov and Dingwell (1996) and developed further by e.g. Alatorre-Ibargüengoitia et al. (2010); Rager et al. (2014); Mayer et al. (2015). The apparatus consists of a large upper chamber at ambient pressure and temperature conditions, and a small high-pressure chamber (autoclave) which is heated and pressurized, usually by Argon gas (Fig. 4 suppl. mat.). The autoclave is separated from the chamber by a series of diaphragms. Controlled rupturing of the diaphragms initiates rapid decompression of the autoclave. A transparent section at the bottom of the large chamber allows monitoring of the sample ejection by a high-speed camera. The ejected material is recovered, and analysed for its shape and grain-size distribution analogous to the samples of the hydrothermal explosions deposit (see sections 4.3 and 4.4). These experiments qualitatively investigate the role of the loose nature of the material involved on the fragmentation and ejection dynamics of explosions. We looked at the changes in grain-size distribution of pre-sieved material, and measured the velocities of ejected particles.

The pre-sieved unconsolidated material from the Gengissig sedimentary succession that served as sample material included all the main components, from lava and scoriaceous clasts to aggregates. Different combinations of grain-sizes were used to investigate the effect on fragmentation and ejection behaviour (Table 2 suppl. mat. and Fig. 6). Cylindrical steel crucibles (34 mm in diameter and 70 mm long) were completely filled with particles of known grain-size. Gentle tapping of the particle-filled crucible ensured comparable conditions in terms of particles amount and porosity for different experiments. Using the weight of the particles and the volume of the crucibles, porosity could be estimated (Table 2 suppl. mat.). A fairly high bulk porosity was obtained due to the use of mainly coarse material, but these conditions were in line with the experiment purpose. After placement in the crucible the samples were placed in water and kept in a moderate vacuum to assure a complete saturation of the porous particles.

The pressure and temperature conditions used in this study represent those of the decompression following the Gengissig drainage. The water height at the craters area dropped ca. 20 m, corresponding to a pressure drop of approximately 0.2 MPa. We assume that the water temperature at the lake bottom corresponds to the boiling temperature under pressure prior to drainage ($\sim$0.3 MPa), which is 133.5 °C (see section 8). The decompression results in the explosive boiling of the water (and so the steam formation), which is driving the explosion and is the same process invoked for the Gengissig case. During experiments the entire pressurization, heating and dwelling process lasted 20–30 min, ensuring the samples reached thermal equilibrium (Fig. 4 suppl. mat.).

6.2.2. Results

The grain-size distribution of the recovered material was analysed and compared to that prior to the experiment. All grain-size distributions of the ejected samples exhibit an increased weight fraction of ash-sized particles (Fig. 6). This may be an indication of fragmentation as well as other size-reducing processes such as disintegration of aggregates. A qualitative morphological analysis was performed on the 180–250 μm fraction of two samples, which contained most of the freshly-fragmented material (Fig. 6a). In this grain-size fraction only minor evidence was found for freshly-formed fractures, possibly due to the lack of fracturing occurring in that grain-size fraction, or due to the lack of fresh material in which fractures could be recognised. Analogous to the analysed particles from the hydrothermal explosion deposits, most clasts consist of aggregates (Fig. 6b, d). These are usually composed either by fragments of crystals and glassy parts in a matrix of alteration minerals, or by clusters of alteration minerals only (Fig. 6a, d). The remaining particles in that size range are mainly glass fragments covered by a blanket of micron or sub-micron sized alteration minerals (Fig. 6c).

The ejection velocity of the gas-particle mixture was obtained from high-speed video recordings of each experiment. Results showed in Fig. 7 indicate that the clasts were ejected with velocities of up to 100 m/s. In all the experiments for particles smaller than 1 mm the initial ejection speed is of 60–100 m/s, whereas the first larger particles (>2 mm) are ejected later and show a velocity range of 40–50 m/s.

7. Energy considerations

Estimates of the energy associated with these hydrothermal explosions includes the mechanical energy required to produce the

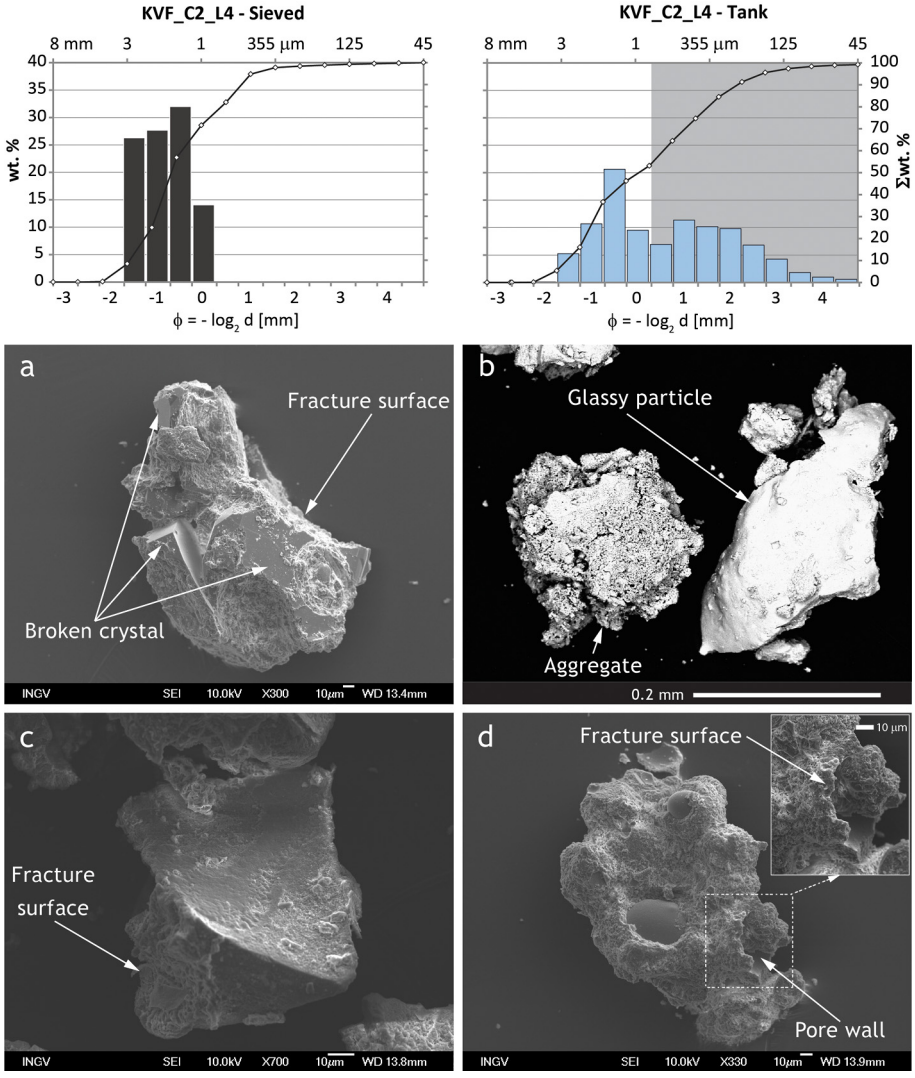

Fig. 6. Above: grain size distribution of pre-selected loose material, before and after decompression experiments. The shaded area highlights the size distribution of the newly-formed particles, which show a peak around 355 µm. Below: field emission scanning electron microscopy (FESEM) images showing: (a) broken crystals in a matrix of alteration minerals showing fresh fractures; (b) aggregates and glass particle; (c) altered blocky shaped glass fragment showing fresh fractures; (d) alteration minerals aggregate with fresh fractures around some of the pore walls.

observed cratering and ejecta, balanced with the energy available for the explosive processes.

The calculation of available energy is based on the thermodynamic change of the geothermal system before and after drainage pressure failure (Muffler et al., 1971; Mastin, 1995). The estimated energy is approximate as the rock properties prior to the explosion and the depth of the craters are imperfectly known. Additionally the irregular crater shape, assumed here to be circular/elliptical, and errors in the deposit volume calculations (Table 1), add a certain degree of uncertainty to our estimation. For each observed crater we assumed a conical vent. The diameter and estimated volume was used to calculate the focal depth of the explosion (or the deepest level from which rock material was removed) defined as the tip of the downwards pointing cone. The estimated depths range between 11 and 23 m (Table 1).

As described in section 3 these explosions were triggered by a decrease in confining pressure as a consequence of Gengissig lake drainage (1637 to 1607 m a.s.l. in ca. 10–15 hrs; Fig. 8a). The pressure failure caused boiling in the surficial geothermal reservoir and thereby explosions (Fig. 8b–d). The area where the explosions developed was roughly ca. 20 m below the lake level. A maximum

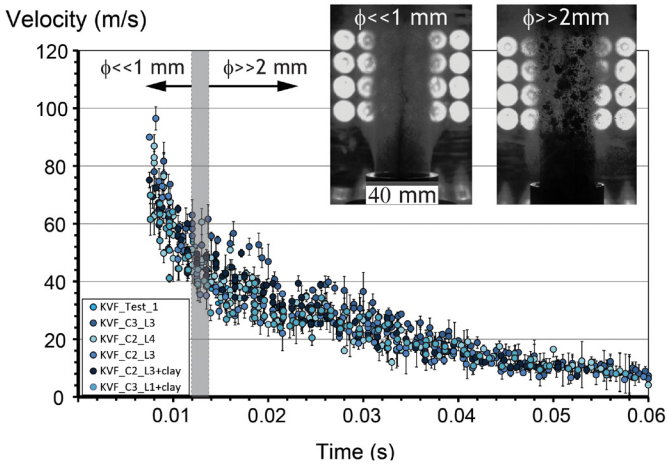

Fig. 7. Ejection velocities of particles with time, measured using image analysis of high-speed camera footage. Within inlet the difference in the ejected particle size is shown.

drainage of 30 m was instead reached in the deepest, southern part of the Gengissig lake (Figs. 1 and 8a).

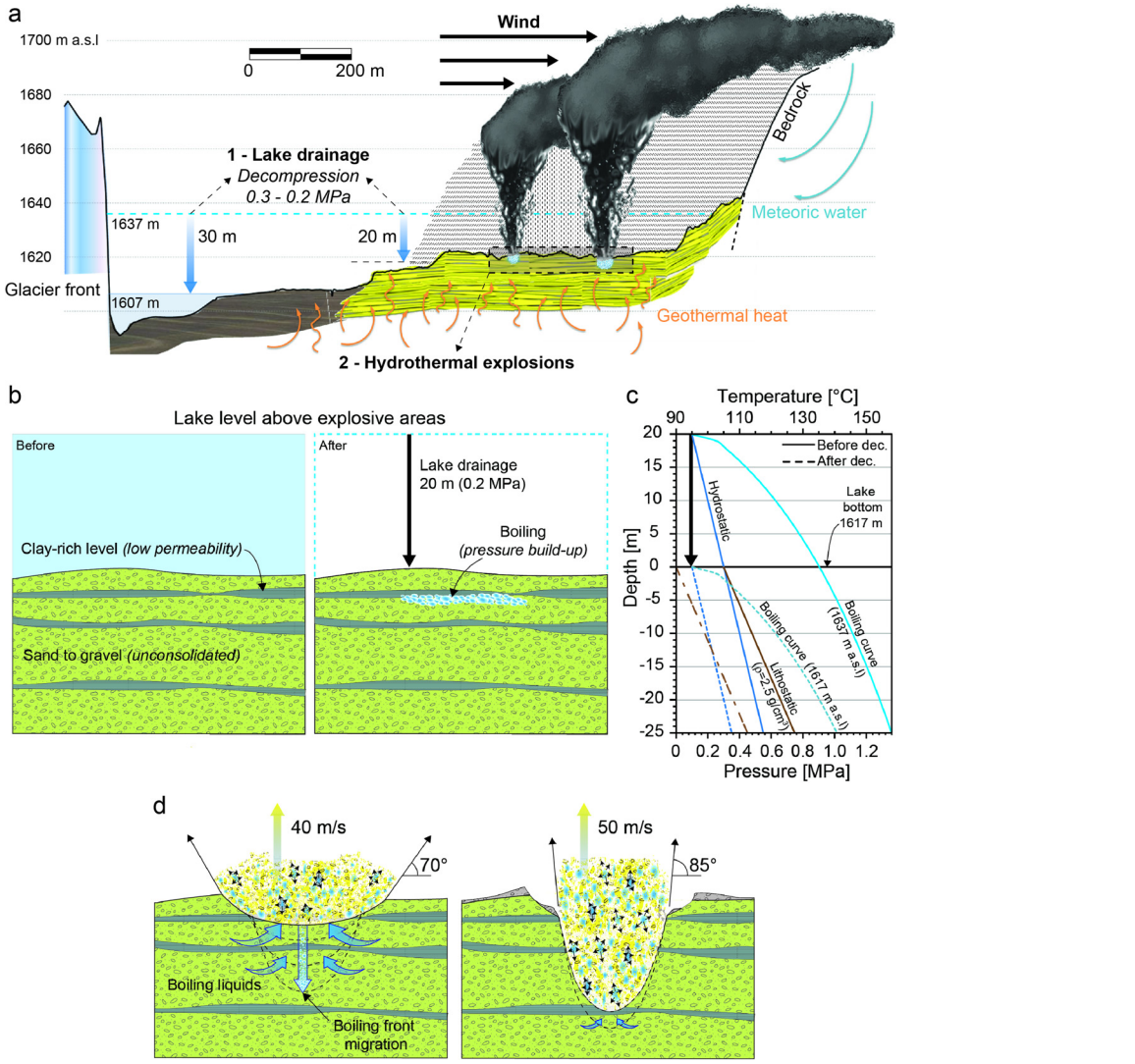

Fig. 8. Sketch showing the setting before and after the lake drainage. (a) Profile across Gengissig, based on kinematic GPS collected 12 days after the explosions. (b–d) Conceptual model of the hydrothermal explosions evolution: (b) lake drainage (pressure failure) and boiling initiation; (c) hydrostatic, lithostatic and boiling point temperature before and after lake drainage; (d) explosion caused by clay layer failure and subsequent pressure release and progressive downwards propagation of boiling front. See text for more explanation.

The drainage of the glacially-dammed lake reduced the effective confining pressure on the sub-lacustrine hot-spring system (corresponding to the craters area as mapped from the field; see section 4.2) by the equivalent of a ca. 20 m water column (approximately 0.2 MPa), and the controlling boiling point curve became relative to a free-water level at 1617 m a.s.l. Here, the declining water level results in higher steam pressures developing close to the ground surface as boiling conditions descend deeper into the reservoir (Muffler et al., 1971; Browne and Lawless, 2001). The temperature of the lake bed at points of thermal up-flow is assumed to be 133.5 °C. Similarly, at a depth of 25 m, slightly below the maximum focal depth, it is assumed to be 155.5 °C. Parts of the affected system may not have been at maximum permissible temperatures, and so the average initial temperature is conservatively assumed to be 144.5 °C (Fig. 8c). Thus the hydrothermal explosion process assumes water at an initial temperature of 144.5 °C and pressure of 0.3 MPa which flashes to steam, cooling to approximately 94.87 °C (the boiling point of water at 1617 m a.s.l.). At the same time, additional heat is transferred from rock debris to the water, causing further steam production. Therefore, assuming an isolated system, a reservoir pore volume of 28% (averaged value for sand-gravel mixed deposits), a heat of vapourisation for water of 2.26×10^6 J/kg, and an isenthalpic and irreversible depressurization, the energy available for craterisation and ejection is (Muffler et al., 1971):

$$\Delta E_{\mathrm{Th}} = [m_r \times c_r \times \Delta t] + \left[X \times m_w \times \left(U^{t1}_{\mathrm{water}} - U^{t2}_{\mathrm{steam}}\right)\right] + \left[(1-X) \times m_w \times \left(U^{t1}_{\mathrm{water}} - U^{t2}_{\mathrm{water}}\right)\right] \quad (3)$$

X = steam fraction (calculated by using:
$\Delta t \times (m_w \times c_w + m_r \times c_r) = X \times m_w \times L$);
m_r–m_w = rock–water mass (kg);
c_r = rock specific heat of 900 J/kg × °C (assuming an average lava composition);
U^{t1-t2} = internal energy before and after explosions.

Thus we estimated a thermal energy ranging between 7×10^9 J and 1×10^{11} J for the different craters (Fig. 9 and Table 1).

Craterization energy is assessed using the cube-root similarity rule of explosion dimensions (Nordyke, 1962; Sato and Taniguchi, 1997; Goto et al., 2001). This method, which assumes a scaling relationship between the craters formed by individual explosions and explosive energy and depth, has been proved to be valid on a wide range of scale and holds well for surficial explosions (Lee and Mazzola, 1989; Sato and Taniguchi, 1997 and

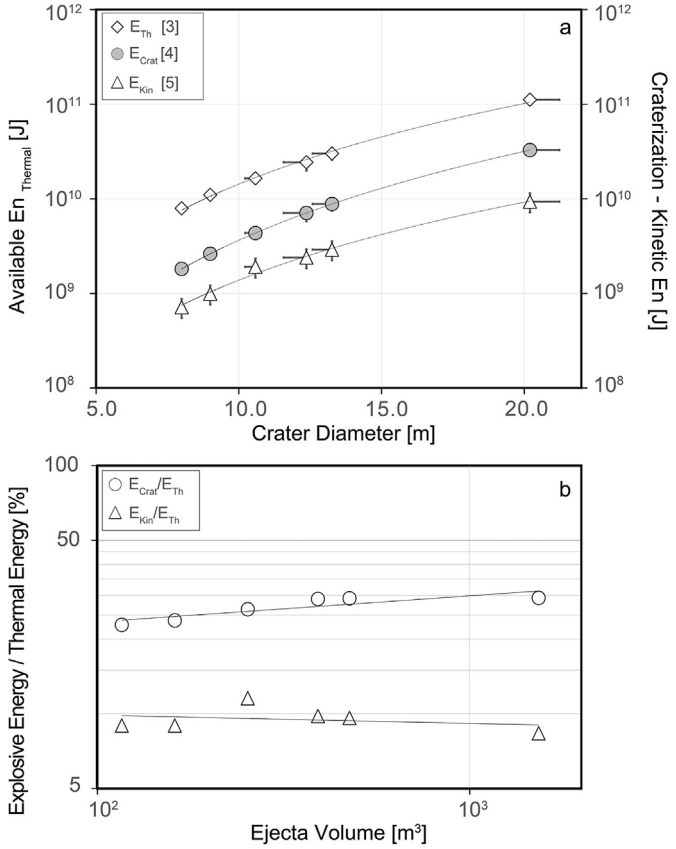

Fig. 9. (a) Semi-log plot showing thermal (E_{Th}), craterisation (E_{Crat}) and kinetic (E_{Kin}) energy vs. crater size (see also Table 1). (b) Log–log plot showing the ratio of craterisation and kinetic energy to thermal energy.

reference therein). Valentine et al. (2012) point out that final crater size is not a good indicator of the energy of individual explosions, especially for large scale maar-like events, since the final size is the result of multiple explosions in the subsurface and collapses of the crater rim. However, good agreement is shown between the energy–crater size ratio of the studied hydrothermal explosions, and that of field-based explosion experiments performed in loose material (Goto et al., 2001; Taddeucci et al., 2013; Graettinger et al., 2014). We suggest that the similarity rule is applicable to our case because of the loose nature of the material involved and the shallow depths of explosion. Furthermore in-situ observation of the fresh morphology soon after the event suggest that little changes in the crater rim shape occurred. Therefore, to calculate the energy we use the similarity rule established by Goto et al. (2001):

$$\log D = 0.32 \times \log E_{Crat} - 2.06 \quad (4)$$

The results for the observed crater diameters (D) indicate an energy (E_{Crat}) ranging approximately from 2×10^9 J and 3×10^{10} J (Table 1).

The kinetic energy required to transport ejecta was also assessed. With a well-constrained mass of the ejected material, and neglecting the energy dissipated in the accompanying seismic wave and air blast, we calculate the kinetic energy of the ejected projectiles using:

$$E_{kin} = 1/2 \times M \times V^2 \quad (5)$$

Based on the distribution of the ballistically ejected material (<10 cm in size and deposited within a range of 50 to 100 m from the craters), and optimum angles of 70–85°, this yields an initial velocity varying between 40–50 m/s assuming zero drag (Fagents and Wilson, 1993). By using the field-measured density (1.1 g/cm^3) and the volume estimated at each crater we estimated an energy range between 7×10^8 and 9×10^9 J (Table 1).

Finally, we evaluate the energy conversion ratio (hereafter ECR: the ratio of the mechanical energy to the thermal energy), which is an important parameter to define how efficiently the available energy budget is partitioned. Fig. 9 shows both the ratio of craterisation and kinetic energy over thermal energy plotted against ejecta volume. The ECR of thermal to craterisation energy ranges from ca. 23–30% whereas the kinetic energy associated with the transport of ejected material is on the order of ca. 8.5–12%.

8. Discussion

8.1. Explosion mechanism and dynamic

The drainage of Gengissig lake on 15th to 16th of August 2013 caused a decrease in confining pressure beneath the lake bed (4–8 Pa/s), which triggered rapid boiling in the surficial geothermal reservoir (Fig. 8a–c), and lead to several hydrothermal explosions through coarse unconsolidated sediments interbedded with clay or clay-rich levels (seen in crater successions). As permeability in unconsolidated clastic sediments is known to scale with grain size, we can assume that the coarse (sand to gravel) sections are sufficiently permeable to dissipate the pressure perturbation caused by the lake drainage. In contrast, permeability measurements of the clay-rich levels resulted in low to very low values (1.2×10^{-17} m^2), which excludes dissipation of the pressure over the time of lake drainage and suggests that clay-rich levels can have acted as capping layers in the Gengissig hydrothermal explosions. Explosions are triggered if the residual pressure developed below such a layer is sufficient to cause the failure of the capping clay level, and results in a sudden pressure drop below them (Fig. 8). However, as the clay layers are only 0.15–0.2 m thick and interbedded in coarse unconsolidated sediments, we expect them to behave in a weak manner. When failure occurs, the generated boiling-front penetrates downwards into the geothermal reservoir, followed by the explosion front (McKibbin et al., 2009), where the steam expands, fragmenting and dispersing the surrounding material (Fig. 8c–d). Explosion continues until the rate of groundwater boiling decreases and steam expansion ceases to provide sufficient energy to eject rocks from the crater (Fig. 8d). The explosions at Gengissig occurred on the north-western side of the lake, where the presence of fumarole systems and boiling pools indicate a local high heat flow. Besides favouring pressurization, the low-permeable clay level might helped maintaining liquids at boiling conditions during the decompression phase by hindering the migration of cold fluids into the explosion sites.

Based on the debris distribution, and assuming the downward migration of the explosive process, we speculate that an initial shallow phase of the explosion produced a funnel-shaped cloud with clasts ejected at a low angle. This may have evolved into a more elongated fan with a higher ejection angle as the focal depth of explosion deepened (Fig. 8c–d). The ejection dynamics inferred here are based on similarities with the jet shape produced during natural eruptions (Yokoo et al., 2002), and on field-based explosion experiments using loose material at varying shallow depths (Ohba et al., 2002; Valentine et al., 2012; Taddeucci et al., 2013; Graettinger et al., 2014).

Seismic data indicate that the explosive activity lasted approximately 40–50 s. Assuming that many short-time scale explosions occurred, of which the most intense shaped the final crater size (Goto et al., 2001), we lack sufficient resolution to constrain the duration of explosions at each crater (at least 9). Thus the continuous signals recorded indicate that the explosive events may have

occurred sequentially or with a very short interval, possibly of seconds, at the different craters.

Results from decompression experiments indicate the production of "fresh" fine particles. Comparison of the morphology of the newly-formed material with the pristine component would suggest that the majority of the fresh fragments derive from dismembered aggregates. Furthermore, the ejection velocities of the particles obtained experimentally yield good agreement with the velocities estimated from field data. The very fine material is ejected at higher velocities (100 m/s) compared to the lapilli-sized clasts (>2 mm). The two velocity regimes fit well with the proposed scenario and can explain the different ejection modes inferred from the deposits. Thus the fine particles are ejected at higher elevation and caught by the wind, whereas the coarse material is emplaced ballistically around the crater area.

8.2. Energy budget and partitioning

The assessed thermal energy available in the hydrothermal system at Gengissig is in the order of 10^{11} J, consistent with the estimates made for similar-sized (i.e. crater size, deposit area and estimated volumes) events in Yellowstone (Muffler et al., 1971; Morgan et al., 2009). The energy required to excavate the ejected material (approx. 10^4 m^3) at Gengissig has been estimated to be approximately 5.9 J/cm^3 (ECR of ca. 30%). This value fits well with the range of 3 to 15 J/cm^3 estimated from field-based explosion experiments performed in loose material (ECR between 30 and 70%; Valentine et al., 2012; Graettinger et al., 2014), and also with the value of 8.4 J/cm^3 (ECR of ca. 40%) estimated by Muffler et al. (1971). The ECR from thermal to kinetic energy, assessed for comparable hydrothermal eruptions occurring in cemented, mostly consolidated or highly fractured rocks, ranges between 0.1 and 6% (Browne and Lawless, 2001). However, we estimated a values of ECR between 8.5 and 12% for the Gengissig hydrothermal explosions (Fig. 9). We relate this highly efficient conversion to the loose nature of the sedimentary material involved, as the energy partitioning into fragmentation and viscoelastic deformation depends strongly on media properties (Murphey and Vortman, 1961; Goto et al., 2001; Ohba et al., 2002; Valentine et al., 2012). Thus, most of the mechanical energy has been used in the erosive process of craterisation and ejection of material, with only a minor (not quantifiable) amount consumed in fragmentation, as inferred from the particles morphology. A very small portion (ECR << 0.01%) is converted into seismic energy, while the remaining energy was dissipated as heat, generating steaming over days and weeks following the explosions.

8.3. Broader implications

Our study on the Gengissig explosions has broader implications in terms of hazard management in Iceland and understanding other similar events. In terms of hazard management, the seismic data recorded in this event provide insight into how similar events occurring in other remote, subglacial areas in Iceland might be detected. In cases where a subglacial jökulhlaup path is long, signals of this kind may occur before the onset of water drainage outside the glacier edge. This has practical implications for hazards, since the drainage of subglacial lakes has on several occasions caused damage to roads, bridges and other infrastructure in Iceland.

In terms of understanding other similar events better, we note that in the case of Gengissig the occurrence of explosions during the re-equilibration of the geothermal system to lower pressure, and hence temperature, depended on (1) the timescale of this destabilization process, (2) presence of liquids close to the boiling point at sub-surface, and (3) existence, and variability (thickness and strength), of a near-surface low-permeable layer. These can be generally considered the main factors controlling the response of a reservoir to rapid decompression, which does not always result in an explosion.

9. Conclusions

The 16th August 2013 hydrothermal explosions at Gengissig lake were caused by a pressure failure that followed lake drainage. The approach used here to investigate hydrothermal explosions allowed us to constrain different aspects of these phenomena combining 1) field analyses, 2) seismic signals and 3) laboratory experiments. Our detailed mapping of the deposits soon after their emplacement yields good estimations of the ejected mass and volume, which are also reasonably consistent to theoretical models, making the Gengissig explosions a rare example of small hydrothermal explosions where full characterization of the events is possible.

The comparison of the collected data with analytical modelling yields a robust constraint on the energies released by these small-size explosions. The characterization of the stratigraphic sequence involved in the explosions provided an opportunity to understand the effect of the host rock lithology, which here appear to control the explosion dynamics and energy partitioning.

Furthermore the seismic energy released in this well-constrained event may be used to detect similar hydrothermal explosions occurred in the past jökulhlaups. If validated, use of seismic data might provide a proxy for future events and used in hazard management.

Acknowledgements

CM, BS, MTG, HIR, and KS acknowledge the support of the European Commission (FP7-MC-ITN, grant number 289976: NEMOH). KSV, MTG and TD acknowledge support from EC FP7 grant number 308377, FUTUREVOLC. BS and DBD acknowledge support from the EC FP7 under grant agreement No. 282759 (VUELCO). CM, BS and DBD acknowledge support from EC FP7 grant agreement No. 308665 (MED-SUV). DBD acknowledges the support of ERC Advanced Grant No. 247076 (EVOKES). Thanks to all the people from the Vatnajökull 2014 spring expedition, in particular to Herdís Schopka, Baldur Bergsson, Melissa Pfeiffer, Katerina Mistal and Ísleifur Friðriksson for the support in the field. Tinna Jónsdóttir and Alison Graettinger are acknowledged for fruitful discussions on particle shapes. Thanks to the INGV (Istituto Nazionale di Geofisica e Vulcanologia) HP–HT Laboratory of Experimental Volcanology and Geophysics of Rome for the use and the help with the field emission scanning electron microscopy (FESEM). We further acknowledge the constructive criticisms and comments from Matthew Sweeney, two anonymous reviewers and the editor, Tamsin Mather.

Appendix A. Supplementary material

Supplementary material related to this article can be found online at http://dx.doi.org/10.1016/j.epsl.2015.11.043.

References

Alatorre-Ibargüengoitia, M.A., Scheu, B., Dingwell, D.B., Delgado-Granados, H., Taddeucci, J., 2010. Energy consumption by magmatic fragmentation and pyroclast ejection during vulcanian eruptions. Earth Planet. Sci. Lett. 291 (1), 60–69. http://dx.doi.org/10.1016/j.epsl.2009.12.051.

Alidibirov, M., Dingwell, D.B., 1996. Magma fragmentation by rapid decompression. Nature 380 (6570), 146–148. http://dx.doi.org/10.1038/380146a0.

Barberi, F., Bertagnini, A., Landi, P., Principe, C., 1992. A review on phreatic eruptions and their precursors. J. Volcanol. Geotherm. Res. 52, 231–246. http://dx.doi.org/10.1016/0377-0273(92)90046-G.

Breard, E.C.P., Lube, G., Cronin, S.J., Fitzgerald, R., Kennedy, B., Scheu, B., Montanaro, C., White, J.D.L., Tost, M., Procter, J.N., Moebis, A., 2014. Using the spatial distribution and lithology of ballistic blocks to interpret eruption sequence and dynamics: August 6 2012 Upper Te Maari eruption, New Zealand. J. Volcanol. Geotherm. Res. 286, 373–386. http://dx.doi.org/10.1016/j.jvolgeores.2014.03.006.

Browne, P.R.L., Lawless, J.V., 2001. Characteristics of hydrothermal eruptions, with examples from New Zealand and elsewhere. Earth-Sci. Rev. 52, 299–331. http://dx.doi.org/10.1016/S0012-8252(00)00030-1.

Carrivick, J.L., Russell, A.J., Tweed, F.S., 2004. Geomorphological evidence for Jökulhlaup from Kverkfjöll volcano, Iceland. Geomorphology 63, 81–102. http://dx.doi.org/10.1016/j.geomorph.2004.03.006.

Choy, G.L., Boatwright, J.L., 1995. Global patterns of radiated seismic energy and apparent stress. J. Geophys. Res. 100, 18205–18228.

Choy, G.L., McGarr, A., Kirby, S.H., Boatwright, J.L., 2006. An overview of the global variability in radiated energy and apparent stress. In: Abercrombie, R., McGarr, A., Kanamori, H., Di Toro, G. (Eds.), Earthquakes, Radiated Energy and the Physics of Earthquake Faulting. In: AGU Geophys. Monogr. Ser., vol. 170, pp. 43–57.

Cousins, C.R., Crawford, I.A., Gunn, M., Carrivick, J.L., Harris, J.K., Kee, T.P., Karlsson, M., Carmody, L., Cockell, C., Herschy, B., et al., 2013. Mars analogue glaciovolcanic hydrothermal environments in Iceland: detection and implications for astrobiology. J. Volcanol. Geotherm. Res. 256, 61–77. http://dx.doi.org/10.1016/j.jvolgeores.2013.02.009.

de Marsily, G., 1986. Quantitative Hydrogeology. Groundwater Hydrology for Engineers. Academic Press, London.

Fagents, S.A., Wilson, L., 1993. Explosive volcanic eruptions. VII. The ranges of pyroclasts ejected in transient volcanic eruptions. Geophys. J. Int. 113, 359–370. http://dx.doi.org/10.1111/j.1365-246X.1993.tb00892.x.

Goto, A., Taniguchi, H., Yoshida, M., Ohba, T., Oshima, H., 2001. Effects of explosion energy and depth to the formation of blast wave and crater: field explosion experiment for the understanding of volcanic explosion. Geophys. Res. Lett. 28, 4287–4290. http://dx.doi.org/10.1029/2001GL013213.

Graettinger, A.H., Valentine, G.A., Sonder, I., Ross, P.S., White, J.D.L., Taddeucci, J., 2014. Maar-diatreme geometry and deposits: subsurface blast experiments with variable explosion depth. Geochem. Geophys. Geosyst. 15 (3), 740–764. http://dx.doi.org/10.1002/2013GC005198.

Gudmundsson, M.T., Högnadóttir, Th., 2009. Jökullón í Vestari Kverkfjöllum, þróun og jökulhlaupahætta (in Icelandic). Report for the Road Administration, Iceland.

Gudmundsson, M.T., Einarsson, B., Oddsson, B., 2013. Hlaup og gufusprengingar (jökulhlaup and phreatic explosions) í Kverkfjöllum í ágúst 2013. Jökull 63, 149–151.

Hurst, T., Jolly, A.D., Sherburn, S., 2014. Precursory characteristics of the seismicity before the 6 August 2012 eruption of Tongariro volcano, North Island, New Zealand. J. Volcanol. Geotherm. Res. 286, 294–302. http://dx.doi.org/10.1016/j.jvolgeores.2014.03.004.

Jóhannsson, 1959. Haustferð á Vatnajökul 1959. Jökull 9, 41–42.

Jolly, A.D., Jousset, P., Lyons, J.J., Carniel, R., Fournier, N., Fry, B., Miller, C., 2014. Seismo-acoustic evidence for an avalanche driven phreatic eruption through a beheaded hydrothermal system: an example from the 2012 Tongariro eruption. J. Volcanol. Geotherm. Res. 286, 331–347. http://dx.doi.org/10.1016/j.jvolgeores.2014.04.007.

Kato, A., Terakawa, T., Yamanaka, Y., Maeda, Y., Horikawa, S., Matsuhiro, K., Okuda, T., 2015. Preparatory and precursory processes leading up to the 2014 phreatic eruption of Mount Ontake, Japan. Earth Planets Space 67, 111. http://dx.doi.org/10.1186/s40623-015-0288-x.

Kilgour, G., Manville, V., Della Pasqua, F., Reyes, A.G., Graettinger, A.H., Hodgson, K.A., Jolly, A.D., 2010. The 25 September 2007 eruption of Mt. Ruapehu, New Zealand: directed ballistics, Surtseyan jets, and ice-slurry lahars. J. Volcanol. Geotherm. Res. 191, 1–14. http://dx.doi.org/10.1016/j.jvolgeores.2009.10.015.

Lee, C.K.B., Mazzola, T.A., 1989. Ejecta scaling law for craters in dry alluvial sites. J. Geophys. Res. 94, 17595–17605. http://dx.doi.org/10.1029/JB094iB12p17595.

Lube, G., Breard, E.C.P., Cronin, S.J., Procter, J.N., Brenna, M., Moebis, A., Pardo, N., Stewart, R.B., Jolly, A., Fournier, N., 2014. Dynamics of surges generated by hydrothermal blasts during the 6 August 2012 Te Maari eruption, Mt. Tongariro, New Zealand. J. Volcanol. Geotherm. Res. 286, 348–366. http://dx.doi.org/10.1016/j.jvolgeores.2014.05.010.

Mastin, L., 1995. Thermodynamics of gas and steam-blast eruptions. Bull. Volcanol. 57, 85–98. http://dx.doi.org/10.1007/BF00301399.

Mayer, K., Scheu, B., Gilg, H.A., Heap, M.J., Kennedy, B.M., Lavallée, Y., Letham-Brake, M., Dingwell, D.B., 2015. Experimental constraints on phreatic eruption processes at Whakaari (White Island volcano). J. Volcanol. Geotherm. Res. 302, 150–162. http://dx.doi.org/10.1016/j.jvolgeores.2015.06.014.

McKibbin, R., Smith, T.A., Fullard, L., 2009. Components and phases: modeling progressive hydrothermal eruptions. ANZIAM J. 50, 365–380. http://dx.doi.org/10.1017/S144618110900011X.

Morgan, L.A., Shanks, W.C., Pierce, K.L., 2009. Hydrothermal Processes Above the Yellowstone Magma Chamber: Large Hydrothermal Systems and Large Hydrothermal Explosions. Geological Society of America, Boulder, Colo.

Muffler, L.J.P., White, D.E., Truesdell, A.H., 1971. Hydrothermal explosion craters in Yellowstone National Park. Geol. Soc. Am. Bull. 82, 723–740. 10.1130/0016-7606(1971)82[723:HECIYN]2.0.CO;2.

Murphey, B.F., Vortman, L.J., 1961. High-explosive craters in desert alluvium, tuff, and basalt. J. Geophys. Res. 66 (10), 3389–3404. http://dx.doi.org/10.1029/JZ066i010p03389.

Nordyke, M.D., 1962. An analysis of cratering data from desert alluvium. J. Geophys. Res. 67, 1965–1974. http://dx.doi.org/10.1029/JZ067i005p01965.

Ohba, T., Taniguchi, H., Oshima, H., Yoshida, M., Goto, A., 2002. Effect of explosion energy and depth on the nature of explosion cloud: a field experimental study. J. Volcanol. Geotherm. Res. 115, 33–42. http://dx.doi.org/10.1016/S0377-0273(01)00307-9.

Óladóttir, B.A., Larsen, G., Sigmarsson, O., 2011. Holocene volcanic activity at Grímsvötn, Bárdarbunga and Kverkfjöll subglacial centres beneath Vatnajökull, Iceland. Bull. Volcanol. 73, 1187–1208.

Ólafsson, M., Torfason, H., Grönvold, K., 2000. Surface exploration and monitoring of geothermal activity in the Kverkfjöll geothermal area, central Iceland. Proc. World Geoth. Congr. 2000, 1539–1545.

Pétursson, G.G., Vogfjörd, K.S., 2012. Attenuation relations for near- and far field peak ground motion (PGV, PGA) and new magnitude estimates for large earthquakes in SW-Iceland. Icelandic Meteorological Report, no. VÍ 2009-012, ISSN 1670-8261, 43 pp.

Pyle, D.M., 1989. The thickness, volume and grain-size of tephra fall deposits. Bull. Volcanol. 51, 1–15. http://dx.doi.org/10.1007/BF01086757.

Rager, A.H., Smith, E.I., Scheu, B., Dingwell, D.B., 2014. The effects of water vaporization on rock fragmentation during rapid decompression: implications for the formation of fluidized ejecta on Mars. Earth Planet. Sci. Lett. 385, 68–78. http://dx.doi.org/10.1016/j.epsl.2013.10.029.

Sato, H., Taniguchi, H., 1997. Relationship between crater size and ejecta volume of recent magmatic and phreato-magmatic eruptions: implications for energy partitioning. Geophys. Res. Lett. 24, 205–208. http://dx.doi.org/10.1029/96GL04004.

Seki, K., Kanda, W., Ogawa, Y., Tanbo, T., Kobayashi, T., Hino, Y., 2015. Imaging the hydrothermal system beneath the Jigokudani valley, Tateyama volcano, Japan: implications for structures controlling repeated phreatic eruptions from an audio-frequency magnetotelluric survey. Earth Planets Space 67, 6. http://dx.doi.org/10.1186/s40623-014-0169-8.

Smith, T., McKibbin, R., 2000. An investigation of boiling processes in hydrothermal eruptions. In: Proc. World Geotherm. Congr. 2000, vol. 1, pp. 699–704.

Taddeucci, J., Valentine, G.A., Sonder, I., White, J.D.L., Ross, P.S., Scarlato, P., 2013. The effect of pre-existing craters on the initial development of explosive volcanic eruptions: an experimental investigation. Geophys. Res. Lett. 40, 507–510. http://dx.doi.org/10.1002/grl.50176.

Thorarinsson, S., 1953. The Grímsvötn expedition June–July 1953 (Vatnajökulsferð 1953). Jökull 3, 6–22.

Thorarinsson, S., 1968. Vatnajökulsleiðangur 1968. 1.–14. júní. (The Vatnajökull expedition, June 1–14, 1968). Jökull 18, 394–400.

Valentine, G.A., White, J.D.L., Ross, P.S., Amin, J., Taddeucci, J., Sonder, I., Johnson, P.J., 2012. Experimental craters formed by single and multiple buried explosions and implications for volcanic craters with emphasis on maars. Geophys. Res. Lett. 39. http://dx.doi.org/10.1029/2012GL053716.

Vogfjörd, K.C., Bean, M., Roberts, B., Ofeigsson and Guralp Systems Ltd., 2013. Extending Icelandic volcanological network operations into the ice caps. In: EGU General Assembly 2013. Vienna, Austria, 2013, Geophys. Res. Abstr. 15. EGU2013-13319.

Yamamoto, T., 2014. The pyroclastic density currents generated by the September 27, 2014 phreatic eruption of Ontake Volcano, Japan. Bull. Geol. Surv. Jpn. 65 (9), 117–127.

Yokoo, A., Goto, A., Taniguchi, H., Oshima, H., 2002. Energy and depth of Usu 2000 phreatic explosions. Geophys. Res. Lett. 29, 48–51. http://dx.doi.org/10.1029/2002GL015928.